Article

Quantitative Evaluations of Hydrogen Diffusivity in V-X (X = Cr, Al, Pd) Alloy Membranes Based on Hydrogen Chemical Potential

Asuka Suzuki [1],* and Hiroshi Yukawa [2]

[1]   Department of Materials Process Engineering, Graduate School of Engineering, Nagoya University, Furo-cho, Chikusa-ku, Nagoya 464-8603, Japan
[2]   Department of Materials Design Innovation Engineering, Graduate School of Engineering, Nagoya University, Furo-cho, Chikusa-ku, Nagoya 464-8603, Japan; hiroshi@nagoya-u.jp
*   Correspondence: suzuki.asuka@material.nagoya-u.ac.jp

Abstract: Vanadium (V) has higher hydrogen permeability than Pd-based alloy membranes but exhibits poor resistance to hydrogen-induced embrittlement. The alloy elements are added to reduce hydrogen solubility and prevent hydrogen-induced embrittlement. To enhance hydrogen permeability, the alloy elements which improve hydrogen diffusivity in V are more suitable. In the present study, hydrogen diffusivity in V-Cr, V-Al, and V-Pd alloy membranes was investigated in view of the hydrogen chemical potential and compared with the previously reported results of V-Fe alloy membranes. The additions of Cr and Fe to V improved the mobility of hydrogen atoms. In contrast, those of Al and Pd decreased hydrogen diffusivity. The first principle calculations revealed that the hydrogen atoms cannot occupy the first-nearest neighbor T sites (T1 sites) of Al and Pd in the V crystal lattice. These blocking effects will be a dominant contributor to decreasing hydrogen diffusivity by the additions of Al and Pd. For V-based alloy membranes, Fe and Cr are more suitable alloy elements compared with Al and Pd in view of hydrogen diffusivity.

Keywords: hydrogen permeation; vanadium; mobility; chemical potential; first principle calculation

1. Introduction

Hydrogen energy needs to be utilized effectively to realize a decarbonized society [1]. Since hydrogen does not exist as a simple substance in nature, it needs to be manufactured industrially. Even when hydrogen gas is manufactured or generated through any routes, it is necessary to purify the product gas for usage in the fuel cells since it always contains not only hydrogen gas but also by-product gases [2]. Hydrogen gas with high purity is obtained by separation and purification through hydrogen-permeable dense metallic membranes [3]. Pd-based alloy membranes are the most representative metallic membranes used for the purification of hydrogen gas [4,5].

Recently, group 5 metal-based alloy membranes have been developed to avoid using high-cost precious metal Pd. The hydrogen permeability of group 5 metals with a body-centered cubic (BCC) crystal structure is much more superior to Pd and Pd-based alloy membranes [6]. However, group 5 metals have high hydrogen solubility and become significantly brittle under hydrogen atmosphere (hydrogen-induced embrittlement) [7,8]. The presence of the ductile-to-brittle transition hydrogen concentration (DBTC) has been found by small punch testing under hydrogen atmospheres at elevated temperatures [8,9]. The small punch absorption energy of group 5 metals decreases drastically at around 0.2 (H/M). Hydrogen solubility needs to be optimized so that the hydrogen concentration does not exceed 0.2 (H/M) under operating pressure and temperature conditions of metal membranes. The elements with low affinity for hydrogen are usually added to control hydrogen solubility.

Considering the influence of the alloy elements on the microstructure and hydrogen diffusivity, single-phase solid solution alloys are considered to be preferable. To form the solid solution alloys and control hydrogen solubility, alloy elements with large solid solubility limits in base metals are preferable. Among group 5 metals, V forms solid solutions with many elements in wide ranges of alloy compositions. Therefore, various V-based solid solution alloys such as V-Ni [10–12], V-Cr [12], V-Al [12,13], V-Pd [14], V-Fe [15], V-W [16], and V-W-Mo [17] alloys have been investigated. It is more suitable that the alloy elements enhance hydrogen diffusivity in V. It is reported that the addition of Fe to V enhances hydrogen diffusivity below approximately 700 K [15].

In the present study, the hydrogen solubility and permeability of V-Al, V-Cr, and V-Pd alloy membranes were investigated systematically to examine the effects of alloy elements on hydrogen diffusivity quantitatively. The mobility of hydrogen atoms, B, in these alloy membranes was evaluated by the following equation [18]:

$$J = \frac{RTB}{2L} \int_{c_2}^{c_1} c \frac{d \ln\left(P/P^0\right)}{dc} dc = \frac{RTB}{2L} f_{\text{PCT}} \tag{1}$$

This equation is based on the diffusion equation based on the chemical potential of hydrogen [18]. Here, J is hydrogen flux through the membrane, L is the membrane thickness, R is the gas constant, T is absolute temperature, c is hydrogen concentration, c_1 and c_2 are hydrogen concentrations at feed and permeation sides of the membrane, P is hydrogen pressure, P^0 is the standard hydrogen pressure (101325 Pa), and f_{PCT} represents the integral term in Equation (1).

The first principle calculations were also carried out to investigate the interactions between hydrogen atoms and alloy elements in a BCC V crystal lattice.

2. Materials and Methods

2.1. Experimental Procedure

V-4 mol%Cr, V-14 mol%Cr, V-23 mol%Cr, V-5.5 mol%Al, V-16 mol%Al, V-20 mol%Al, V-25 mol%Al, V-10 mol%Pd, and V-15 mol%Pd alloy ingots were melted under an argon gas atmosphere using a tri-arc furnace. The purity of starting materials is 99.9 mass% for vanadium (Taiyo Koko Co., Ltd., Tokyo, Japan), 99.88 mass% for chromium (Tosoh Co., Ltd., Tokyo, Japan), 99.999 mass% for aluminum, and 99.95 mass% for palladium (Tanaka Kikinzoku Kogyo K.K., Tokyo, Japan). The chemical compositions of each sample analyzed by a scanning electron microscopy/energy dispersion X-ray spectroscopy are summarized in Table 1. In the equilibrium phase diagrams for V-Cr, V-Al, and V-Pd binary systems [19–21], these alloys consist of a single phase with a BCC crystal structure. Figure 1 shows the X-ray diffraction (XRD) profiles of these alloys. Only peaks derived from the BCC crystal structure were detected.

Table 1. Chemical compositions of V-Cr, V-Al, and V-Pd alloys analyzed by SEM/EDS analysis.

Sample	Mole Fraction of Alloying Elements (mol%)
V-4Cr	4.3
V-14Cr	13.7
V-23Cr	23.0
V-5.5Al	5.5
V-16Al	15.8
V-20Al	19.9
V-25Al	24.7
V-10Pd	9.8
V-14.5Pd	14.5

The PCT curves of the alloys were measured using a Sieverts-type apparatus to examine hydrogen solubility and to estimate the PCT factor (f_{PCT}). A small bulk cut from the sample ingot was set into a sample cell, and then the sample cell was set on the apparatus and evacuated. The activation process for the sample was carried out before measuring the PCT curves. The detailed activation process applied in this study was given elsewhere [15]. The PCT measurements were carried out at 473~673 K.

The samples for hydrogen permeation tests were fabricated by cutting the as-cast ingots of V-4 mol%Cr, V-14 mol%Cr, V-23 mol%Cr, V-5.5 mol%Al, V-16 mol%Al, V-20 mol%Al, V-25 mol%Al, V-10 mol%Pd, and V-14.5 mol%Pd alloys into disks with approximately 12 mm in diameter using a wire-cut electrical discharge machine (EDM). The damaged surface layer of the disk samples caused by EDM was removed by mechanical polishing with alumina abrasive papers and heat treatment in a vacuum at 1273 K for 24 h. The surfaces of disk samples were treated by mechanical polishing using alumina abrasive papers and buffing with diamond slurry (9 μm and 1 μm). The final thicknesses (L) of each sample were 0.500 mm for V-4 mol%Cr, 0.428 mm for V-14 mol%Cr, 0.521 mm for V-23 mol%Cr, 0.550 mm for V-5.5 mol%Al, 0.562 mm for V-16 mol%Al, 0.425 mm for V-20 mol%Al, 0.504 mm for V-25 mol%Al, 0.521 mm for V-10 mol%Pd, and 0.366 mm for V-14.5 mol%Pd, respectively. A radio-frequency (RF) magnetron sputtering apparatus was used for coating the Pd-27mol%Ag alloy on both sides of the membrane samples. The sputtering was carried out for 180 s at 573 K under Ar gas atmosphere of 1 Pa so that the thickness of the overlayer was approximately 200 nm. The reason why the Pd-Ag alloy was selected for the overlayer instead of pure Pd was given in the previous study [15].

Hydrogen permeability was measured by the gas permeation method applying differential pressures. The G1 grade hydrogen gas was used for the tests. The testing conditions including the temperature and the hydrogen pressures are summarized in Tables 2–4. Detailed methods of the hydrogen permeation test are described in the previous study [22]. To eliminate the effect of the difference in the membrane thickness, the normalized hydrogen flux ($J \cdot L$) was evaluated in this study. Note that the unit of the normalized hydrogen flux in this study is mol H m^{-1} s^{-1} instead of mol H$_2$ m^{-1} s^{-1}.

Table 2. Temperature and pressure conditions of hydrogen permeation tests for V-Cr alloy membranes.

Sample	Temperature, T/K	Hydrogen Pressure, P/kPa	
		Feed	Permeate
V-4 Cr (L = 0.500 mm)	573	30, 35, 40	
	623	28, 30	
	673	30, 40, 50, 60, 70	
V-14 Cr (L = 0.428 mm)	573	30, 35, 40, 45	
	623	45, 60, 80, 100, 120	10
	673	120, 150, 180, 250, 280	
V-23 Cr (L = 0.521 mm)	573	100, 130, 150, 180, 200	
	623	200, 250, 300, 350, 400, 450, 500	
	673	500, 600, 700, 800, 900	

Table 3. Temperature and pressure conditions of hydrogen permeation tests for V-Al alloy membranes.

Sample	Temperature, T/K	Hydrogen Pressure, P/kPa	
		Feed	Permeate
V-5.5 Al ($L = 0.550$ mm)	573	20	
	623	20, 25	
	673	25, 30, 40, 50, 60, 70	
V-16 Al ($L = 0.562$ mm)	573	30, 40, 50	
	623	30, 40, 50, 80, 100, 130, 150	
	673	50, 100, 150, 180, 200, 250, 300, 350	
V-20 Al ($L = 0.425$ mm)	573	100, 150, 200	10
	623	200, 300, 400, 500	
	673	200, 500, 600, 700, 1000	
V-25 Al ($L = 0.504$ mm)	573	300, 400, 500, 600, 700, 800	
	623	200, 300, 400, 500, 600, 700, 800, 900	
	673	300, 500, 800, 1000	

Table 4. Temperature and pressure conditions of hydrogen permeation tests for V-Pd alloy membranes.

Sample	Temperature, T/K	Hydrogen Pressure, P/kPa	
		Feed	Permeate
V-10 Pd ($L = 0.521$ mm)	573	100, 130, 150, 180, 200, 230, 250	
	623	250, 300, 350, 400, 450, 500	
	673	200, 300, 400, 500, 600, 700, 800, 900	10
V-14.5 Pd ($L = 0.366$ mm)	573	100, 130, 150, 180, 200, 230, 250, 300	
	623	300, 350, 400, 450, 500	
	673	300, 400, 500, 600, 700, 800, 900	

2.2. First Principle Calculation

Interactions between alloy elements and hydrogen atoms in vanadium (BCC) crystal lattice were investigated by the first principle calculations based on the density functional theory (DFT). Supercell models were constructed by $2 \times 2 \times 2$ of the BCC crystal structure of vanadium. The atom at the center of the supercell was substituted for alloy elements (X = Cr, Pd, Al, and Fe). This model is denoted as $V_{15}X_1$ assuming V-X solid solution alloy. One hydrogen atom was put into the first-, second-, and third-nearest neighbor tetrahedral interstitial sites (T1, T2, and T3 sites) of the X atom. These models are denoted as $V_{15}X_1H_1$(T1), $V_{15}X_1H_1$(T2), and $V_{15}X_1H_1$(T3) and are treated as hydrogen solid solution phases with the hydrogen concentration of 0.0625 (H/M). The detailed model explanation is given in the previous report [23].

The CASTEP code was used for geometry optimizations and energy calculations for all these models [24]. A plane-wave pseudopotential method implemented in the CASTEP code is applied. The pseudopotential used in this study was the Vanderbilt ultra-soft type. The Perdew–Burke–Ernzerhof generalized gradient approximation (GGA-PBE) was applied. The cutoff energy and k-point grid were set at 400 eV and $8 \times 8 \times 8$, respectively.

Firstly, $V_{15}X_1$ models were fully optimized, and the lattice parameters of $V_{15}X_1$ models were calculated. The lattice parameters of the $V_{15}X_1H_1$(T1) model were estimated using the lattice parameters of $V_{15}X_1$ models and considering the volume expansion induced by the occupation of hydrogen atoms into the BCC crystal lattice (approximately 2.6 Å³ per 1 (H/M)) [25]. The optimized $V_{15}X_1$ models were isotopically expanded, and a hy-

drogen atom was inserted into the T1 site. Then, the constructed $V_{15}X_1H_1(T1)$ models were geometrically optimized. Only the positions of the atoms inside the supercell were optimized while the lattice parameters were constrained.

The changes in the total energy induced by hydrogen insertion into T1, T2, and T3 sites were calculated with the following equation:

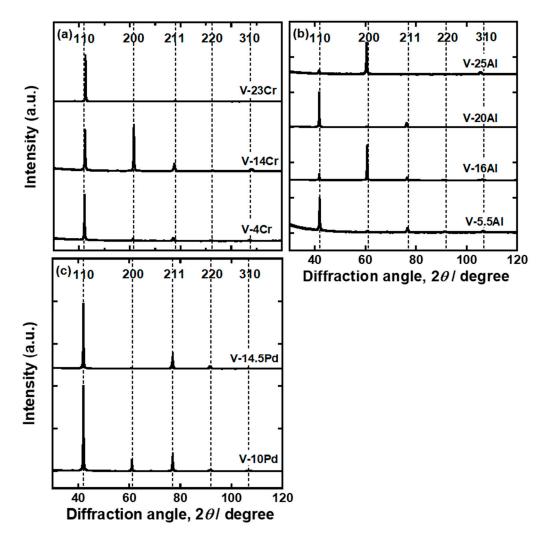$$\Delta E = E(V_{15}X_1H_1) - E(V_{15}X_1) - \frac{1}{2}E(H_2) \tag{2}$$

where $E(V_{15}X_1H_1)$, $E(V_{15}H_1)$, and $E(H_2)$ are the total energies of $V_{15}X_1H_1$, $V_{15}H_1$, and H_2 models, respectively.
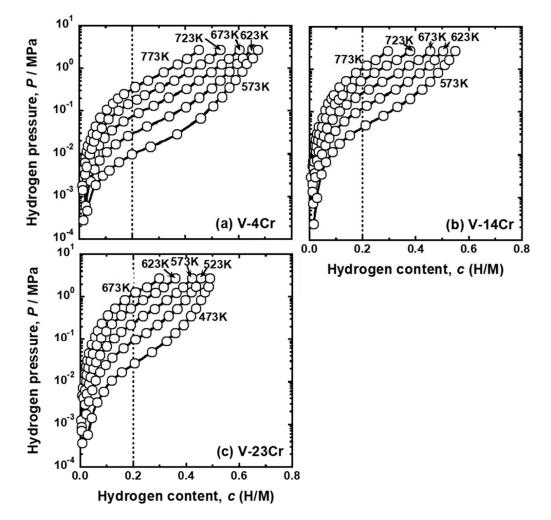
3. Results

3.1. Experimental Results

Figure 1 shows the X-ray diffraction (XRD) profiles of these alloys. Only peaks derived from the BCC crystal structure were detected, suggesting that all the samples are composed of single phases with BCC crystal structures.

Figure 1. X-ray diffraction (XRD) profiles for (**a**) V-Cr, (**b**) V-Al, and (**c**) V-Pd alloys fabricated in this study.

Figure 2 shows the pressure-composition isotherms (PCT curves) of (a) V-4 mol%Cr, (b) V-14 mol%Cr, and (c) V-23 mol%Cr alloys. The V-Cr alloys exhibited PCT curves with inverse sigmoid shapes. There were clear inflection points even when Cr concentration

was 23 mol%. Hydrogen solubility decreased with increasing temperature, indicating that dissolutions of hydrogen into V-Cr alloys were exothermic reactions.

Figure 2. Pressure-composition isotherms (PCT curves) of (**a**) V-4mol%Cr, (**b**) V-14mol%Cr, and (**c**) V-23mol%Cr alloys.

Figure 3 presents the PCT curves of (a) V-5.5 mol%Al, (b) V-16 mol%Al, (c) V-20 mol%Al, and (d) V-25 mol%Al alloys. The V-5.5 mol%Al alloy also exhibited typical PCT curves with inverse sigmoid shapes. However, in the PCT curves of V-16 mol%Al, V-20 mol%Al, and V-25 mol%Al alloys, clear inflection points were not observed. For example, although the PCT curve for V-20 mol% Al at 573 K was an upward convex curve at low pressure and a downward convex curve at high pressure, its boundary was not clear. These alloys had a steeper slope around the inflection points compared with V-Cr alloys. As the temperature increased, the PCT curves shifted toward the upper left region. Thus, the dissolution of hydrogen into V-Al alloys was also exothermic reactions.
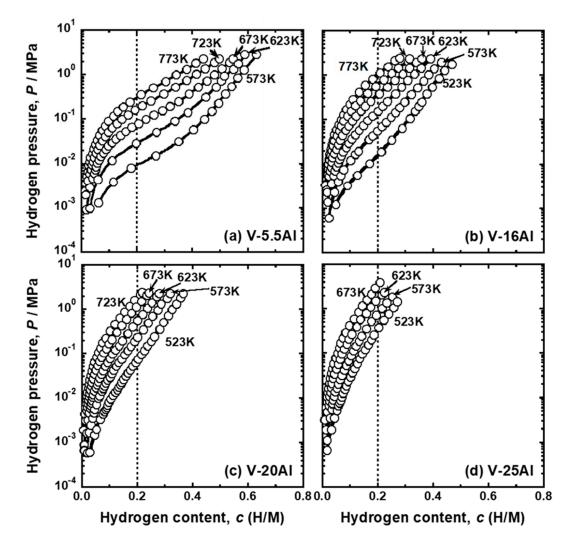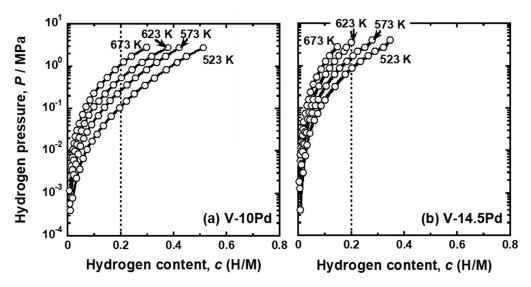
Figure 3. PCT curves of (**a**) V-5 mol%Al, (**b**) V-15 mol%Al, (**c**) V-20 mol%Al, and (**d**) V-25 mol%Al alloys.

Figure 4 shows the PCT curves of (a) V-10 mol%Pd and (b) V-14.5 mol%Pd alloys. The PCT curves of these alloys were upward convex curves under the whole hydrogen pressure region tested in this study (approximately up to 2 MPa). The temperature dependence of the PCT curves for these alloys also indicated that exothermic reactions took place upon hydrogen uptake into them.
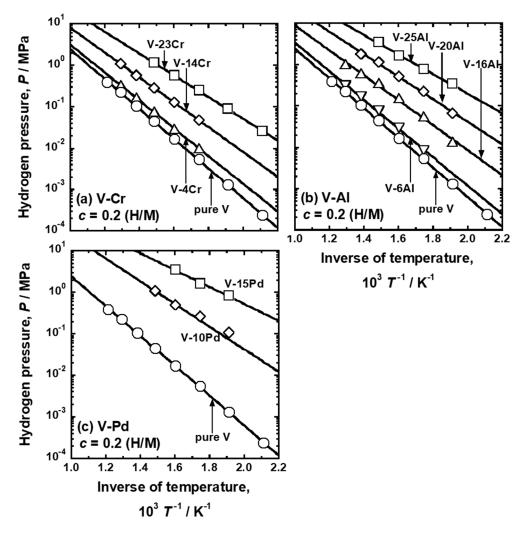
The pressure of gaseous hydrogen in equilibrium with hydrogen atoms in metals and alloys with the hydrogen concentration of 0.2 (H/M), i.e., DBTC (P (0.2)), were quantified from the PCT curves shown in Figures 2–4. Figure 5 shows the change in P (0.2) for (a) V-Cr, (b) V-Al, and (d) V-Pd alloys with reciprocal temperature. For comparison, the results for pure V [15] are also shown in the figure. The addition of Cr, Al, and Pd increased P (0.2). The logarithmic hydrogen pressure decreased linearly as the inverse of temperature increased. The linear correlations in Figure 5 are known as the van't Hoff equation in Equation (3).

$$\ln \frac{P(c)}{P^0} = \frac{2\Delta \overline{H}(c)}{RT} - \frac{2\Delta \overline{S}(c)}{R} \tag{3}$$

where $P(c)$ is the pressure of gaseous hydrogen in equilibrium with hydrogen atoms in metals and alloys with the hydrogen concentration of c. $\Delta \overline{H}(c)$ and $\Delta \overline{S}(c)$ are the partial molar enthalpy and entropy changes of hydrogen for forming hydrogen solid solution phase with hydrogen concentration of c. From the regression lines in Figure 5, $\Delta \overline{H}(0.2)$ and $\Delta \overline{S}(0.2)$, which are denoted as $\Delta \overline{H}_{0.2}$ and $\Delta \overline{S}_{0.2}$ in the present study, were quantified.
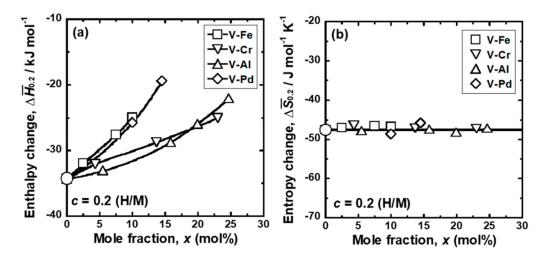
Figure 4. PCT curves of (**a**) V-10 mol%Pd and (**b**) V-14.5 mol%Pd alloys.

Figure 5. Relationship between the equilibrium hydrogen pressure (*P*) at 0.2 (H/M) and the inverse of temperature (T^{-1}) for (**a**) V-Al, (**b**) V-Cr, and (**c**) V-Pd alloys. The values for pure V [15] are also shown in the figures.
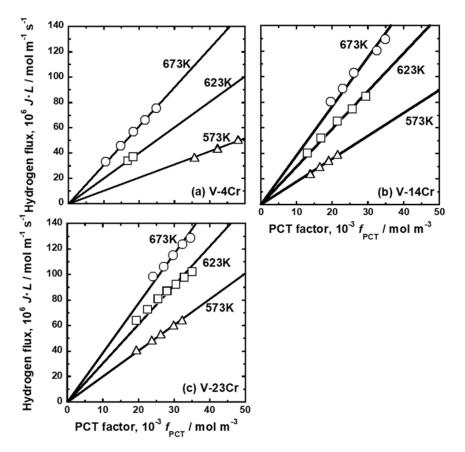
Figure 6 presents the changes in (a) $\Delta\overline{H}_{0.2}$ and (b) $\Delta\overline{S}_{0.2}$ for V-Cr, V-Al, and V-Pd alloys with mole fractions of each alloy element. For comparison, the values for pure V and V-Fe alloys are also shown in the figure [15]. $\Delta\overline{H}_{0.2}$ increased as the mole fractions of each alloy element increased (Figure 6a) because Fe, Cr, Al, and Pd exhibit lower affinity to hydrogen than V. The additions of Fe and Pd increased the partial molar enthalpy change more largely than those of Cr and Al. $\Delta\overline{H}_{0.2}$ increased almost linearly with the mole fractions of Fe and Cr, but it increased along downward convex curves with increasing Al and Pd mole fractions. When the amount of alloy elements was small, V-Al alloy showed the lowest $\Delta\overline{H}_{0.2}$ among those elements. However, the value for the V-Al alloy became higher that than for the V-Cr alloy when the mole fraction was over approximately 20 mol%.
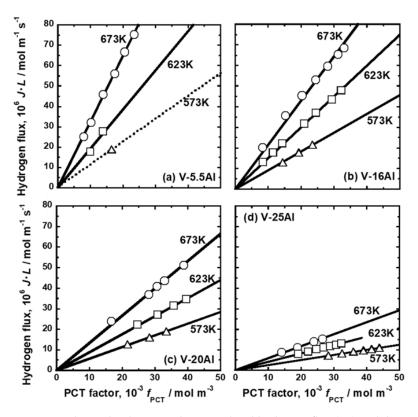

Figure 6. Changes in the (**a**) partial molar enthalpy change ($\Delta\overline{H}_{0.2}$) and (**b**) partial molar entropy change ($\Delta\overline{H}_{0.2}$) for hydrogen dissolution at 0.2(H/M), as a function of the mole fraction (x) of alloying elements. For comparison, the results of pure V and V-Fe alloys are also shown in the figure [15].

In contrast, $\Delta\overline{S}_{0.2}$ was almost constant at approximately -47 J mol H^{-1} K^{-1} (-94 J mol H_2^{-1} K^{-1}) and independent of types and additive amount of alloy elements. The absolute value of the partial molar entropy was close to the entropy of hydrogen gas in the standard state ($\sim$130 J mol H_2^{-1} K^{-1}) [26], indicating that the partial molar entropy change is mainly attributable to the loss of hydrogen gas with high entropy. Thus, the alloying effects on hydrogen solubility can be understood by $\Delta\overline{H}_{0.2}$.
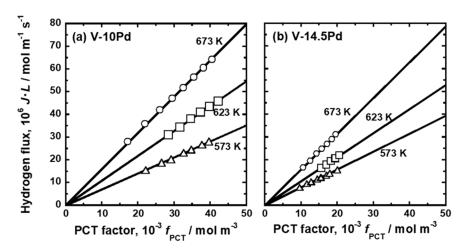
The PCT curves in Figures 2–4 were used to quantify the PCT factors (f_{PCT}) in Equation (1) under the conditions listed in Table 2. A detailed explanation of the way to quantify f_{PCT} is given elsewhere [27]. Figures 7–9 present the relationship between normalized hydrogen flux ($J \cdot L$) and f_{PCT} for V-Cr, V-Al, and V-Pd alloys. As shown in these figures, there are almost linear correlations between $J \cdot L$ and f_{PCT}. The slope of the regression lines increased with the increasing temperature and mole fraction of alloy elements. It is noted that the addition of Al to V obviously reduced the slope of the regression lines, which is a different trend from V-Cr alloy membranes.

Figure 7. Relationship between the normalized hydrogen flux ($J \cdot L$) and the PCT factor (f_{PCT}): (**a**) V-4 mol%Cr, (**b**) V-14 mol%Cr, and (**c**) V-23 mol%Cr.

Figure 8. Relationship between the normalized hydrogen flux ($J \cdot L$) and the PCT factor (f_{PCT}): (**a**) V-5 mol%Al, (**b**) V-16 mol%Al, (**c**) V-20 mol%Al, and (**d**) V-25 mol%Al.

Figure 9. Relationship between the normalized hydrogen flux ($J \cdot L$) and the PCT factor (f_{PCT}): (**a**) V-10 mol%Pd and (**b**) V-15 mol%Pd.

The mobility of hydrogen atoms (B) was estimated from the slopes of the regression lines in Figures 7–9. B in each alloy at each temperature is summarized in Table 5. For comparison, B in pure Pd and Pd-23 Ag alloy [28] is also shown in the Table. Figure 10 presents an Arrhenius plot of B in (a) V-Cr, (b) V-Al, and (c) V-Pd alloy membranes. For comparison, the hydrogen mobility in pure V is also shown in the figure [15]. The logarithmic mobility decreased almost linearly with increasing reciprocal temperature, indicating that the temperature dependence on B was described by the Arrhenius equation as indicated in Equation (4).

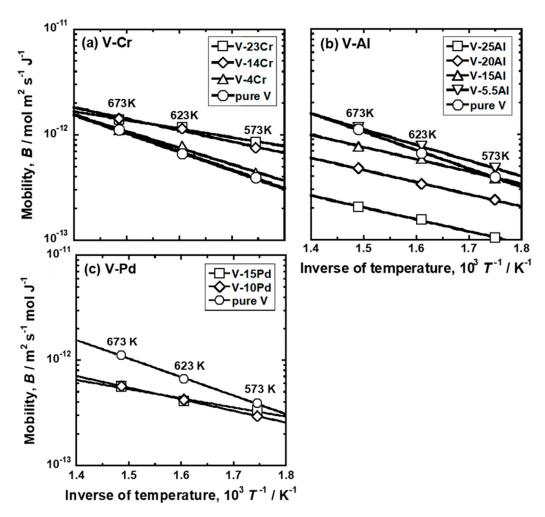$$B = B_0 \exp\left(-\frac{Q}{RT}\right) \qquad (4)$$

where Q is the activation energy required for hydrogen to diffuse, and B_0 is the pre-exponential factor. The addition of Cr to V increased hydrogen mobility in the range of 573–673 K (Figure 10a). The mobility increased significantly especially at lower temperatures by adding Cr. The addition of 5.5 mol% Al to V also increased the mobility slightly at lower temperatures (Figure 10b). However, the mobility decreased by adding Al further. It is noted here that the regression lines of V-16 mol%Al, V-20 mol%Al, and V-25 mol%Al alloys were almost parallel. The addition of Pd to V decreased the mobility of hydrogen atoms in the range of 573–673 K (Figure 10a).

Q and B_0 for each alloy were quantified based on Equation (4) and are summarized in Table 6. For comparison, Q and B_0 for pure Pd and Pd-23 Ag [28] in similar temperature ranges are also shown in the Table. Figure 11 presents changes in (a) Q and (b) B_0 with the mole fraction of each alloy element. For comparison, the results of pure V and V-Fe alloy membranes [15] are shown in the figure. Q decreased almost linearly with the mole fractions of Fe, Pd, and Cr (Figure 11a). Among these elements, the addition of Fe decreased Q the most sharply. The addition of Al to V exhibited an anomalous effect on Q. Q decreased almost linearly when the Al mole fraction was up to around 16 mol% but became almost constant when the Al mole fraction was over 16 mol%. In contrast, the logarithmic B_0 decreased almost linearly with the mole fraction of all the alloy elements. The additions of Fe and Pd decreased B_0 more sharply than those of Al and Cr.

Table 5. Mobility of hydrogen atoms quantified from the slope of the regression lines shown in Figures 7–9.

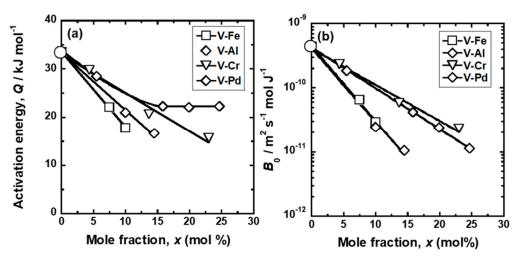| Sample	Temperature, T/K	Mobility, 10^{13} B/mol m^2 s^{-1} J^{-1}
V-4 Cr	673	11.0
	623	7.8
	573	4.4
V-14 Cr	673	14.3
	623	11.4
	573	7.5
V-23 Cr	673	13.8
	623	11.7
	573	8.5
V-5.5 Al	673	11.5
	623	7.7
	573	4.8
V-16 Al	673	7.6
	623	5.8
	573	3.8
V-20 Al	673	4.7
	623	3.4
	573	2.4
V-25 Al	673	2.0
	623	1.6
	573	1.0
V-10 Pd	673	5.7
	623	4.2
	573	3.0
V-14.5 Pd	673	5.6
	623	4.1
	573	3.3
Pure Pd [28]	673	10.0
	573	6.0
Pd-23 Ag [28]	673	8.3
	623	6.4
	573	4.5

Figure 12 presents the relationship between logarithmic B_0 and linear Q. As the data points are plotted in the upper left region, hydrogen diffusivity is higher. There is a roughly positive correlation between logarithmic B_0 and linear Q, and both Q and logarithmic B_0 decreased by adding alloy elements (i.e., the plots move toward the lower left region in the figure). In particular, the results of pure V, V-Fe alloy, and V-Cr alloy are located almost on a single line (the broken line in the figure). The linear correlation between Q and logarithmic B_0 is known as the Meyer–Neldel rule [29]. The plot for V-5.5Al is located on the line, but the results of V-Al alloy with higher Al mole fractions deviate from the line. The plots are located below the broken line and drop vertically with constant Q in the figure. In addition, the results for V-Pd alloys are also located below the broken line. These results indicate that the hydrogen diffusivity in V-Al and V-Pd alloys is lower than that in V-Fe and V-Cr alloys.
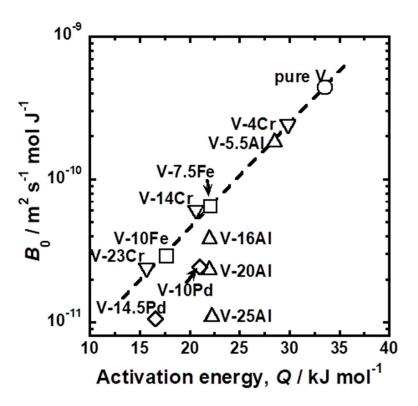
Figure 10. Arrhenius plots of the mobility for hydrogen diffusion in (**a**) V-Cr, (**b**) V-Al, and (**c**) V-Pd alloys. For comparison, the results of pure V are also shown in the figure [15].

Table 6. Mobility of hydrogen atoms quantified from the slope of the regression lines shown in Figure 10.

Sample	Temperature Range	Pre-Exponential Factor, $10^{11} B_0$/mol m^2 s^{-1} J^{-1}	Activation Energy, E/kJ mol^{-1}
V-4 Cr		23.3	29.8
V-14 Cr	573~673 K	5.9	20.6
V-23 Cr		2.3	15.6
V-5.5 Al		18.9	28.5
V-16 Al	573~673 K	4.0	22.0
V-20 Al		2.4	22.0
V-25 Al		1.1	22.2
V-10 Pd	573~673 K	2.4	21.0
V-14.5 Pd		1.1	16.6
Pure Pd [28]	423~673 K	1.4	14.9
Pd-23 Ag [28]	373~673 K	7.3	24.4

Figure 11. Changes in the (**a**) activation energy (Q) and (**b**) pre-exponential factor (B_0) for hydrogen diffusion as a function of the mole fraction (x) of alloying elements. The values for pure V and V-Fe [15] are also shown in the figure.

Figure 12. Relationship between the pre-exponential factor (B_0) and the activation energy for hydrogen diffusion (E) in pure V and various V-based alloys.

3.2. First Principle Calculations

Figure 13 shows the (a,b) $V_{15}Cr_1H_1$(T1) and (c,d) $V_{15}Pd_1H_1$(T1) models (a,c) before and (b,d) after geometry optimizations. In the case of the $V_{15}Cr_1H_1$(T1) model, the V and Cr atoms around the hydrogen atoms were relaxed slightly, but the hydrogen atoms still occupied the T1 site of Cr. The hydrogen atom moved slightly to the position of Cr (Figure 13a,b), indicating attractive interactions operating between hydrogen and Cr atoms. These results are similar to the geometry optimized $V_{15}Fe_1H_1$(T1) model reported in the literature [23]. In contrast, in the case of the $V_{15}Pd_1H_1$(T1) model, it is interesting that the hydrogen atom in the $V_{15}Pd_1H_1$(T1) model moved from the T1 site to the second-nearest neighbor T site (T2 site) of Pd. The Pd in BCC V exhibits a strong repulsive interaction

to hydrogen atoms, although pure Pd with a face-centered cubic (FCC) crystal structure exhibits high affinity for hydrogen. Similar geometry optimizations were reported in the $V_{15}Al_1H_1$(T1) model [23].
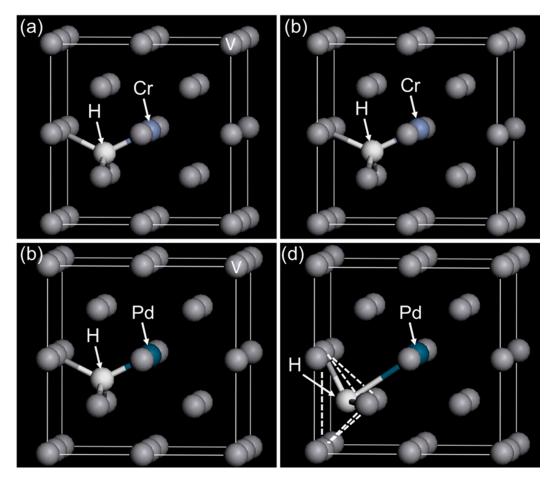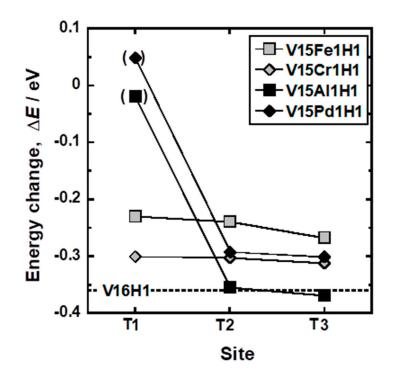

Figure 13. (**a,b**) $V_{15}Cr_1H_1$ (T1) and (**c,d**) $V_{15}Pd_1H_1$ models (T1) (**a,c**) before and (**b,d**) after geometry optimizations.

Figure 14 shows the total energy change (ΔE) for the insertion of a hydrogen atom into the T1, T2, and T3 sites of alloy elements (Fe, Al, Cr, and Pd). Here, the hydrogen atoms in $V_{15}Al_1H_1$ and $V_{15}Pd_1H_1$ models were constrained not to move to the T2 site. Therefore, the total energy change of $V_{15}Al_1H_1$ (T1) and $V_{15}Pd_1H_1$ (T1) models (in parentheses) cannot be directly compared with those of other models. The total energy change of the $V_{16}H_1$ model was approximately -0.36 eV, which is in good agreement with the experimental partial molar enthalpy change of hydrogen for hydrogen dissolution (-0.32 eV H atom^{-1}) [25]. Replacing the central V atom with Cr or Fe atom increased the total energy changes to approximately -0.25 eV and -0.30 eV. The total energy decreased slightly as the distance of hydrogen atoms from Fe or Cr atoms increased, but the energy level of the $V_{15}X_1H_1$ (T3) model is still comparable to that of the $V_{15}X_1H_1$ (T1) model. These results suggest that the additions of Fe or Cr to V increased the potential of hydrogen atoms in V uniformly, which would coincide with the linear increase in $\Delta \overline{H}_{0.2}$ of V-Fe and V-Cr alloys (Figure 6). The total energy changes of $V_{15}Al_1H_1$ (T1) and $V_{15}Pd_1H_1$ (T1) models (denoted in parentheses) are around 0 eV and much higher than those of other models. It is noted here that the total energy changes of $V_{15}Al_1H_1$ (T2 and T3) and $V_{15}Pd_1H_1$ (T2 and T3) models are comparable to those of $V_{16}H_1$ and $V_{15}Cr_1H_1$ models, respectively, indicating that the strong repulsive interactions between H and Al or Pd are localized only near these elements.
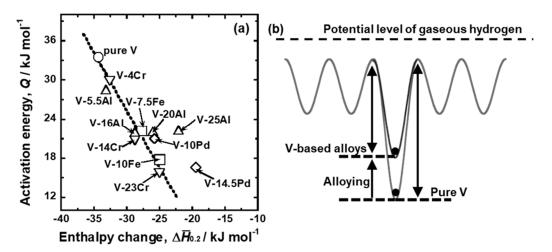
Figure 14. Total energy change (ΔE) for insertion of a hydrogen atom into the T1, T2, and T3 sites of alloying elements (Fe, Al, Cr, and Pd).

4. Discussion

The additions of Cr, Al, and Pd to V decreased the activation energy required for hydrogen to diffuse (Q) (Figure 11a). Similar results are also reported that the additions of alloy elements with lower affinity to hydrogen to group 5 metals decrease Q. For example, the additions of W, Mo, and Ru to Nb decrease the activation energy required for hydrogen to diffuse [30]. It is understood that the mitigation of diffusion barriers is caused by the increase in the potential of the hydrogen atoms at interstitial sites of the BCC Nb crystal lattice [31]. The additions of W, Mo, and Ru with lower affinity to hydrogen than Nb increase the potential of hydrogen atoms in Nb. The potential of the hydrogen atoms at interstitial sites can be understood by the equilibrium hydrogen pressure: higher hydrogen pressure indicates that hydrogen atoms are presented at shallow potential valleys in metals and alloys. The additions of Cr, Al, and Pd increased the equilibrium hydrogen pressure (Figure 5).

It was hypothesized that the activation energy required for hydrogen to diffuse decreases due to the increase in the potential of hydrogen in the BCC V crystal lattice. The increase in the equilibrium hydrogen pressure is attributable to that in the partial molar enthalpy change for forming hydrogen solid solution ($\Delta \overline{H}_{0.2}$) (Figure 6). In order to verify this hypothesis quantitatively, the change in Q was plotted as a function of $\Delta \overline{H}_{0.2}$ in Figure 15a. There is a trend that Q decreased with increasing $\Delta \overline{H}_{0.2}$. The plots for most of the alloys, except for V-14.5 mol%Pd and V-25 mol% Al alloys, are aligned on a line (broken line in the figure). These results support the hypothesis that the increase in the potential of hydrogen in the V crystal lattice by adding alloy elements with lower affinity to hydrogen contributes dominantly to the decrease in Q, as illustrated schematically in Figure 15b. The plots for V-14.5 mol%Pd and V-25 mol% Al alloys are located above the broken line, indicating that another mechanism acts so as not to decrease the activation energy by the additions of Pd and Al to V.
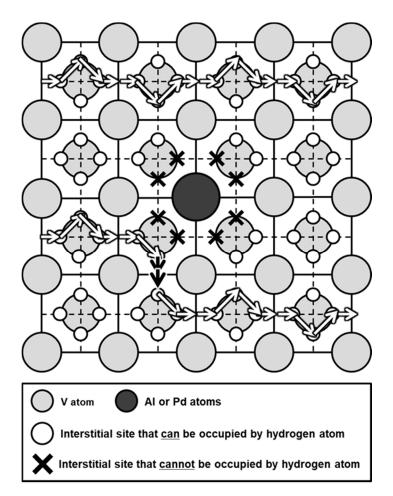
Figure 15. (**a**) Relationship between the activation energy for hydrogen diffusion (Q) and the partial molar enthalpy change of hydrogen for forming hydrogen solid solution with 0.2 (H/M) ($\Delta \overline{H}_{0.2}$) and (**b**) schematic illustration showing the potential level of a hydrogen atom at an interstitial T site in pure V and V-based alloys.

It is reported that the addition of Al to V above 20 mol% decreased hydrogen permeability significantly [13]. Transmission electron microscopy (TEM) observations revealed the presence of some precipitates in the V-30 mol% Al alloy in crystal grains and at grain boundaries and sub-boundaries. However, the amount of those precipitates is too small to explain the significant reduction in the hydrogen permeability above 20 mol% Al, suggesting that the reason for the phenomenon lies in the matrix of V-Al solid solution [13]. In other words, the significant decrease in hydrogen diffusivity in V-Al and V-Pd alloys in the present study, as well as the significant reduction in hydrogen permeability of V-Al alloys in the previous study, may be caused by the interactions between alloy elements and hydrogen atoms in the BCC V crystal lattice.

The first principle calculations revealed that hydrogen atoms could not occupy the first-nearest neighbor T sites (T1 sites) of Al [23,32] and Pd (Figure 13) atoms in BCC V due to strong repulsive interactions. This strong repulsive interaction acted only when the hydrogen atoms occupied the T1 sites of Al and Pd in BCC V (Figure 14). These results are experimentally supported by the PCT curves of V-Al alloys (Figure 3): the slope of the PCT curves of V-16 mol%Al, V-20 mol%Al, and V-25 mol%Al was significantly sharp, and hydrogen concentrations in the high hydrogen pressure region were low compared with V-Cr alloys.

The T1 sites neighboring Al or Pd atoms are blocked by strong repulsive interactions with hydrogen. This blocking effect of Al or Pd atomsdecreases hydrogen diffusivity (Figures 10 and 12). Figure 16 presents a schematic illustrations of (001) plane projection on a BCC crystal lattice. Arrows represent the jumps of hydrogen atoms between adjacent interstitial T sites. Hydrogen atoms cannot jump to the T sites near Pd and Al atoms represented by X symbols in Figure 16. Then, hydrogen atoms need to diffuse while bypassing around Pd or Al atoms (black arrows in Figure 16). As a result, diffusion distance becomes longer, and the apparent mobility of hydrogen atoms decreases.

Figure 16. Schematic illustrations of (001) plane projection on a body-centered cubic (BCC) crystal lattice. Arrows represent the jumps of hydrogen atoms between adjacent interstitial sites.

Both Al and Pd in BCC V inhibit the diffusion paths of hydrogen atoms by blocking the T1 sites but have different effects on hydrogen diffusivity. The addition of a larger amount of Al to V does not decrease the activation energy required for hydrogen to diffuse while decreasing the pre-exponential factor (Figures 11 and 12). The addition of Pd to V decreases both the activation energy and the pre-exponential factor (Figure 11), whereas the pre-exponential factor of V-Pd alloys decreases with the activation energy required for hydrogen to diffuse significantly compared with V-Fe and V-Cr alloys (Figure 12). One of the possible reasons for the difference is the short-range ordering of Al in BCC V. In the present study, all the V-Al alloys were composed of a single phase with the BCC crystal structures, as identified with XRD measurements (Figure 1). However, the presence of the ordered phase with A15 or B2 crystal structures in V-rich V-Al alloys below approximately 873 K was suggested in the previous studies [20]. Although such phases were not detected in the present study, Al in BCC V might be ordered in a short range. In such a case, hydrogen atoms could be present in almost the same potential valley even at high Al concentration. Then, the activation energies are almost constant regardless of the Al concentration. In contrast, no ordered phase has been suggested in the V-Pd binary system up to approximately 20 mol%Pd. Pd atoms can substitute V atoms randomly. Even though hydrogen atoms cannot occupy the T1 site of Pd in BCC V, the potential level of the hydrogen atoms in interstitial sites except for the T1 site is increased by the addition of Pd, resulting in a decrease in the activation energy. However, further investigations will be needed to demonstrate the presence or absence of the short-range ordering of alloy elements in BCC V and clarify the difference in the alloying effects of Al and Pd on hydrogen diffusivity in V.

Group 5 metals-based alloy membranes are designed so as to reduce hydrogen solubility for preventing the hydrogen-induced embrittlement while increasing the slope of the PCT curves for enhancing the hydrogen flux [33]. In order to control the PCT curves, the alloy elements with lower affinity to hydrogen than base metal need to be added. V-based solid solution alloy membranes such as V-Fe, V-Cr, V-Al, and V-Pd alloy membranes are widely investigated [12–15]. It is suitable that the alloy elements not only reduce hydrogen solubility but also enhance hydrogen diffusivity. The present study revealed that the alloying effects of Cr and Al on hydrogen solubility were smaller than those of Fe and Pd (Figure 6). In order to reduce hydrogen solubility, a large amount of Cr and Al needs to be added to V compared with Fe and Pd. However, a large amount of Al in V decreases hydrogen diffusivity (Figures 11 and 12) by the blocking effects required for hydrogen to diffuse (Figure 15). Furthermore, the addition of Pd to V reduces hydrogen solubility as much as that of Fe but decreases hydrogen diffusivity (Figures 11 and 12). Thus, Fe and Cr are more suitable alloy elements for V-based alloy membranes than Al and Pd in view of hydrogen diffusivity.

5. Conclusions

In the present study, alloying effects of Cr, Al, and Pd on hydrogen diffusivity in V were estimated quantitatively by quantifying hydrogen mobility and compared with the previously reported results of V-Fe alloy membranes. The additions of Cr and Fe to V enhance hydrogen diffusivity in the temperature range of 573~673 K, whereas those of Al and Pd decrease hydrogen diffusivity. From the correlation between the activation energy required for hydrogen to diffuse and the partial molar enthalpy change of hydrogen for forming hydrogen solid solution, the enhancement in hydrogen diffusivity by the addition of Cr is caused by the increase in the potential of hydrogen atoms in interstitial sites in the BCC V crystal lattice. The first principle calculation revealed that hydrogen atoms can occupy the first-nearest neighbor T site (T1 site) of Cr or Fe in the BCC V crystal lattice but cannot occupy the T1 site of Al or Pd. The blocking effects of Al and Pd inhibit hydrogen diffusion. In view of hydrogen diffusivity, Cr and Fe are more suitable alloy elements for V-based hydrogen-permeable alloy membranes than Al and Pd.

Author Contributions: Original draft writing, review, response, A.S.; Writing (review and editing), H.Y.; Experiments and analysis, A.S.; Discussion and conceptualization; A.S. and H.Y.; Supervision, funding acquisition, H.Y. All authors have read and agreed to the published version of the manuscript.

Institutional Review Board Statement: Not applicable.

Informed Consent Statement: Not applicable.

Conflicts of Interest: The authors declare no conflict of interest.

References

1. Valente, A.; Iribarren, D.; Galvez-Martos, J.-L.; Dufour, J. Robust eco-efficiency assessment of hydrogen from biomass gasification as an alternative to conventional hydrogen: A life-cycle study with and without external costs. *Sci. Total Environ.* **2019**, *650*, 1465–1475. [CrossRef] [PubMed]
2. Cheng, X.; Shi, Z.; Glass, N.; Zhang, L.; Zhang, J.; Song, D.; Liu, Z.-S.; Wang, H.; Shen, J. A review of PEM hydrogen fuel cell contamination: Impacts, mechanisms, and mitigation. *J. Power Sources* **2007**, *165*, 739–756. [CrossRef]
3. Knapton, A.G. Palladium Alloys for Hydrogen Diffusion Membranes a Review of High Permeability Materials. *Platin. Met. Rev.* **1977**, *21*, 44–50.
4. Serra, E.; Kemali, M.; Perujo, A.; Ross, D.K. Metall. Hydrogen and deuterium in Pd-25 pct Ag alloy: Permeation, diffusion, solubilization, and surface reaction. *Metall. Mater. Sci. A* **1998**, *29*, 1023–1028.
5. Buxbaum, R.E.; Kinney, A.B. Hydrogen transport through tubular membranes of palladium-coated tantalum and niobium. *Ind. Eng. Chem. Res.* **1996**, *35*, 530–537. [CrossRef]
6. Dolan, M.D. Non-Pd BCC alloy membranes for industrial hydrogen separation. *J. Membr. Sci.* **2010**, *362*, 12–28. [CrossRef]

7. Gahr, S.; Birnbaum, H.K. Hydrogen embrittlement of niobium-III. High temperature behavior. *Acta Metall.* **1978**, *26*, 1781–1788. [CrossRef]
8. Matsumoto, Y.; Yukawa, H.; Nambu, T. Quantitative evaluation of hydrogen embrittlement of metal membrane defected by in-situ small punch test under hydrogen permeation. *Met. J.* **2010**, *LXIII*, 74–78.
9. Matsumoto, Y.; Yukawa, H.; Nambu, T. Determination of Ductile-to-Brittle Transition Hydrogen Concentrations for V and Nb Alloys using in-situ Small Punch Test. In *Proceedings of the 2nd International Conference Small Sample Test Technics (SSTT2012)*; Matocha, K., Hurst, R., Sun, W., Eds.; OCELOT s.r.o.: Ostrava, Czech Republic, 2012; pp. 132–137.
10. Amano, M.; Komaki, M.; Nishimura, C. Hydrogen permeation characteristics of palladium-plated V-Ni alloy membranes. *J. Less Common Met.* **1991**, *172–174*, 727–731. [CrossRef]
11. Dolan, M.D.; Mclennan, K.G.; Way, J.D. Diffusion of atomic hydrogen through V-Ni alloy membranes under nondilute conditions. *J. Phys. Chem. C* **2012**, *16*, 1512–1518. [CrossRef]
12. Dolan, M.D.; Kellam, M.E.; Mclennan, K.G.; Liang, D.; Song, G. Hydrogen transport properties of several vanadium-based binary alloys. *Int. J. Hydrog. Energy* **2013**, *38*, 9794–9799. [CrossRef]
13. Nishimura, C.; Ozaki, T.; Komaki, M.; Zhang, Y. Hydrogen permeation and transmission electron microscope observations of V-Al alloys. *J. Alloys Compd.* **2003**, *356*, 295–299. [CrossRef]
14. Alimov, V.N.; Busnyuk, A.O.; Notkin, M.E.; Peredistov, E.Y.; Livshits, A.I. Hydrogen transport through V–Pd alloy membranes: Hydrogen solution, permeation and diffusion. *J. Membr. Sci.* **2015**, *481*, 54–62. [CrossRef]
15. Suzuki, A.; Yukawa, H.; Nambu, T.; Matsumoto, Y.; Murata, Y. Quantitative Evaluation of Hydrogen Solubility and Diffusivity of V-Fe Alloys toward the Design of Hydrogen Permeable Membrane for Low Operative Temperature. *Mater. Trans.* **2016**, *57*, 1823–1831. [CrossRef]
16. Yukawa, H.; Nambu, T.; Matsumoto, Y. V-W alloy membranes for hydrogen purification. *J. Alloys Compd.* **2011**, *509*, S881–S884. [CrossRef]
17. Yukawa, H.; Nambu, T.; Matsumoto, Y. Hydrogen solubility and permeability of V-W-Mo alloy membrane for hydrogen separation and purification. *J. Alloys Compd.* **2013**, *580*, S386–S390. [CrossRef]
18. Suzuki, A.; Yukawa, H.; Nambu, T.; Matsumoto, Y.; Murata, Y. Consistent description of hydrogen permeability through metal membrane based on hydrogen chemical potential. *Int. J. Hydrog. Energy* **2014**, *39*, 7919–7924. [CrossRef]
19. Okamoto, H. Supplemental Literature Review of Binary Phase Diagrams: Ag-Li, Ag-Sn, Be-Pu, C-Mn, C-Si, Ca-Li, Cd-Pu, Cr-Ti, Cr-V, Cu-Li, La-Sc, and Li-Sc. *J. Phase Equilibria Diffus.* **2017**, *38*, 70–81. [CrossRef]
20. Murray, J.L. AI-V (Aluminum-Vanadium). *Bull. Alloy Phase Diagr.* **1989**, *10*, 351–357. [CrossRef]
21. Smith, J.F. Pd-V (Palladium-Vanadium). *Bin. Alloy Phase Diagr.* **1990**, *3*, 3062–3065.
22. Nambu, T.; Shimizu, N.; Ezaki, H.; Yukawa, H.; Morinaga, M. Hydrogen Permeation of Pure Niobium Metal in Highly Soluble Hydrogen State. *J. Jpn. Inst. Met.* **2005**, *69*, 841–847. [CrossRef]
23. Kawai, R.; Yukawa, H.; Suzuki, A.; Nambu, T.; Murata, Y. Alloying effects of Fe and Al on formation and decomposition temperatures of vanadium hydride, V_2H. *Int. J. Hydrog. Energy* **2017**, *42*, 22564–22574. [CrossRef]
24. Segall, M.D.; Lindan, P.J.D.; Probert, M.J.; Pickard, C.J.; Hasnip, P.J.; Clark, S.J.; Payne, M.C. First-principles simulation: Ideas, illustrations and the CASTEP code. *J. Phys. Condens. Matt.* **2002**, *14*, 2717–2744. [CrossRef]
25. Fukai, Y. *The Metal-Hydrogen System*; Springer: Berlin/Heidelberg, Germany, 1993; pp. 95–100.
26. Vanmal, H.H.; Buschow, K.H.J.; Miedema, A.R. Hydrogen Absorption in LaNi5 and Related Compounds: Experimental Observations and Their Explanation. *J. Less Common Met.* **1974**, *35*, 65–76. [CrossRef]
27. Suzuki, A.; Yukawa, H. Review for Consistent Analysis of Hydrogen Permeability through Dense Metallic Membranes. *Membranes* **2020**, *10*, 120. [CrossRef]
28. Suzuki, A.; Yukawa, H. Analysis of Reverse Temperature Dependence of Hydrogen Permeability through Pd-X (X=Y, Ho Ni) Alloy Membranes Based on Hydrogen Chemical Potential. *Membranes* **2020**, *10*, 123. [CrossRef] [PubMed]
29. Yelon, A.; Movaghar, B.; Branz, H.M. Origin and consequences of the compensation (Meyer-Neldel) law. *Phys. Rev. B* **1992**, *46*, 12244. [CrossRef]
30. Suzuki, A.; Yukawa, H.; Nambu, T.; Matsumoto, Y.; Murata, Y. Analysis of hydrogen mobility in Nb-based alloy membranes in view of new description of hydrogen permeability based on hydrogen chemical potential. *J. Alloys Compd.* **2015**, *645*, S107–S111. [CrossRef]
31. Zhang, G.X.; Yukawa, H.; Nambu, T.; Matsumoto, Y.; Morinaga, M. Alloying effects of Ru and W on hydrogen diffusivity during hydrogen permeation through Nb-based hydrogen permeable membranes. *Int. J. Hydrog. Energy* **2010**, *35*, 1245–1249. [CrossRef]
32. Lee, Y.S.; Ouyang, C.; Suh, J.-Y.; Fleury, E.; Cho, Y.W.; Shim, J.-H. Role of alloying elements in vanadium-based binary alloy membranes for hydrogen separation. *J. Memb. Sci.* **2012**, *423–424*, 332–341. [CrossRef]
33. Suzuki, A.; Yukawa, H.; Nambu, T.; Matsumoto, Y.; Murata, Y. Analysis of pressure-composition-isotherms for design of non-Pd-based alloy membranes with high hydrogen permeability and strong resistance to hydrogen-induced embrittlement. *J. Memb. Sci.* **2016**, *503*, 110–115. [CrossRef]